Photochemical Micromotor of Eccentric Core in Isotropic Hollow Shell Exhibiting Multimodal Motion Behavior

Jianhua Zhang[a,b], Fangzhi Mou[a,*], Shaowen Tang[a], Joshua E. Kauffman[b], Ayusman Sen[b,*], Jianguo Guan[a,*]

[a]*State Key Laboratory of Advanced Technology for Materials Synthesis and Processing, International School of Materials Science and Engineering, Wuhan University of Technology, 122 Luoshi Road, Wuhan 430070, China*

[b]*Department of Chemistry, The Pennsylvania State University, University Park, PA 16802, USA*

* Correspondence authors: moufz@whut.edu.cn (F. Mou), asen@psu.edu (A. Sen), guanjg@whut.edu.cn (J. Guan)

Keywords: Micromotor, Mass asymmetry, Photocatalysis, Multimodal motions, Diffusiophoresis

ABSTRACT: Adaptive motion behavior in response to different environmental stimuli is ubiquitous in biology and enables creatures to achieve a diversity of complex tasks, but not typically observed in synthetic systems. Here we propose a design of chemically-powered micromotors actively performing multimodal motion behaviors with the external stimulus changing. They have isotropic outer surfaces but inherent inner mass asymmetry, such as eccentric core-in-hollow shell TiO_2 (E-TiO_2) microspheres. Their motion behavior can be spontaneously transformed among random Brownian propulsion (stochastic walk), negative phototaxis (moving against incident light), and negative photogravitaxis (moving against gravity)

when the light intensity, illumination direction, or fuel concentration change. At a low light intensity and/or low H_2O_2 fuel concentration, the E-TiO_2 micromotors perform directional movement away from light based on the dominated diffusiophoresis by the photocatalytic reaction over the isotropic shell. With the increase of light intensity or fuel concentration, there are more and more photons or fuels to reach the eccentric core and the contribution of the photocatalytic reaction over it to the diffusiophoresis gradually becomes dominant. In this case, the E-TiO_2 micromotors perform stochastic walks near the substrate due to their Brownian random rotational reorientations. The micromotors are single component, have low density, and can be synthesized in a large scale and at a low cost. This work will facilitate the development of multifunctional micro/nanomotors with varying behaviors and functions depending on environmental cues, e.g., enabling efficient search and delivery operations.

1. Introduction

Synthetic micro/nanomotors are capable of autonomously moving in liquid media by harvesting energy from surrounding chemical fuels or external fields (light, electric, magnetic, ultrasound, etc.), and have potential applications in sensing, drug delivery, microsurgery, micro/nanoengineering, and pollutant adsorption/degradation [1-7]. In these applications, micro/nanomotors benefit from specific modes of motility, such as random motion, rotation, spiral motion, or directional taxis to accomplish their tasks more efficiently. For example, random motion of micro/nanomotors facilitates sensing and pollutant adsorption/degradation [8-12], while directional taxis enables micro/nanomotors to “seek out” targets and is of special interest in micro/nanoengineering, drug delivery, and microsurgery [13-19]. Moving forward to the next generation of multifunctional motors capable of accomplishing a variety of tasks, the

ability to build-in controllable multimodal motion behavior is critically important [20,21]. For example, Levy walk which is the optimal search strategy adopted by many organisms involves random "diffusion" punctuated by directed motion [22,23]. Herein, we report a new class of eccentric hollow micro/nanomotors that can reversibly switch from random superdiffusive motion to directed taxis, using two different inputs: light and chemical fuel. This behavior may allow the design of robotic systems capable of honing on to a given target area and then efficiently delivering cargoes over that area.

The key principle in designing micro/nanomotors is to introduce either structural asymmetry (asymmetry in chemical composition, geometry, or crystalline phase) or asymmetry in external applied fields (e.g., chemical or light gradient) [24-29]. Based on this design principle, elaborate micro/nanostructures have been designed for higher speed and greater controllability [11,30-37], but tend to perform a single motion behavior. For example, asymmetric multicomponent structures such as Janus microspheres, bimetallic micro/nanorods, and multilayered microtubes [30,38-42], and single-component micro/nanomotors which are based on asymmetry in geometry or the crystalline phase, both hardly show directional motion over a significant length scale due to constant Brownian randomization [32,43-45]. In addition, asymmetric motors in the externally applied field are typically directional [14,46,47].

We have now developed chemically-powered micromotors performing adaptively multimodal motion behaviors, including random propulsion, negative phototaxis, and negative photogravitaxis, when the light intensity, illumination direction, or fuel concentration change. The as-developed micromotors are eccentric core-in-hollow shell (a spherical solid inner core attached to one side of a hollow shell) TiO_2 (E-TiO_2) microspheres, which have an isotropic surface but an anisotropic interior [48-49]. With a relatively low light intensity (I) and/or low

H_2O_2 fuel concentration (C_f), the photocatalytic reaction mainly occurs on the illuminated surface, which makes the E-TiO_2 particles perform directional motion away from light serving as isotropic semiconductor micromotors. Upon increasing I or C_f to a critical value (e.g., $I \geq 150$ mW cm^{-2} or C_f = 5 wt.%), the E-TiO_2 micromotors undergo superdiffusive random motion stemming from the increased contribution of the photocatalytic reaction over the eccentric core to the diffusiophoresis. The as-reported micromotors have advantages of single component, low density, low cost and large-scale preparation. They will facilitate the development of multifunctional micro/nanomachines with intelligent responsive behaviors and functions determined by environmental cues.

2. Experimental section

2.1. Synthesis of E-TiO_2 micromotors

All chemicals were used as received without further purification. E-TiO_2 microparticles were synthesized by a nonaqueous solvothermal process according to a previous report [48]. Typically, 10 mL of acetylacetone (purchased from Sinopharm Chemical Reagent) were dissolved in 40 mL of isopropyl alcohol (purchased from Sinopharm Chemical Reagent) under continuous stirring followed by the rapid addition of 2 mL tetrabutyl titanate (TBT, purchased from Sinopharm Chemical Reagent). After stirring at ambient temperature for 5 minutes, the transparent yellowish mixture was transferred into a 100 mL Teflon-lined stainless-steel autoclave. After treatment at 200 ℃ for 2 h, the precipitate was separated and washed with ethanol and deionized water 2 times, respectively, and kept in water. Then, the microparticle suspension was calcinated at 500 ℃ for 2 h.

2.2. Characterization

Scanning electron microscopy (SEM) images were collected by a Hitachi S-4800 field-emission SEM (Japan) and the transmission electron microscopy (TEM) images were captured by JEM-F200 (Japan). Bruker D8 Advance X-ray diffractometer (Germany) was used to record the X-ray diffraction (XRD) patterns.

2.3. Light-controlled motion

A 50 μL suspension of the E-TiO_2 micromotors was dropped onto a glass slide (Citotest 1A5107), followed by the addition of 50 μL of H_2O_2 fuel solution. The built-in light source (Leica EL6000, Germany) of the optical microscope (Leica DMI 3000B, Germany) can excite at UV wavelengths from 280 to 410 nm with an adjustable intensity from 0 to 590 mW cm^{-2}. In addition, a UV-LED light source (SZ Lamplic Technology, China) with a wavelength of 365 nm with adjustable intensity (0-500 mW cm^{-2}) was set above the substrate with an incident angle of 45°. The motion behavior of the E-TiO_2 micromotors was observed and recorded by optical microscopy at ambient temperature.

2.4. Motion trajectories and velocity analysis

All videos of two-dimensional (2D) planar motions were tracked and analyzed by Video Spot Tracker V08.01 software and ImageJ. The 3D trajectories of photogravitaxis were calculated by the scale variation of the microscopic fine-tuning knob. Specifically, we focused on the top and then the bottom of a 5 μm SiO_2 sphere under the microscope and recorded the respective positions of the tuning knob of the microscope. Then, the stroke of the knob between two positions was scaled into 0.15 μm/step. To track the E-TiO_2 micromotor performing negative

photogravitaxis, the tuning steps were recorded continuously when adjusting the tuning knob to keep the micromotor in focus. The color-coded 2D trajectory plots and velocity data were analyzed by using MATLAB.

2.5. Quantitative detection of dissolved oxygen

A 30 mL aqueous suspension with the E-TiO_2 micromotors (0.001 mg mL^{-1}) and H_2O_2 (0.01 wt %) was put into a 50 mL beaker mounted with the probe for the dissolved oxygen meter (Jenco 9173R, USA). A UV-LED light source (SZ Lamplic Technology, China) with a wavelength of 365 nm was set below the beaker and the light intensity was set to be 50, 150, 250, and 500 mW cm^{-2}. A control experiment with only H_2O_2 (0.01 wt %) was conducted to rule out spontaneous O_2 production. The J_{O_2} from the illuminated surface of the micromotors was calculated according to the following equation [27].

$$J_{O_2} = \frac{(C_t - C_0) - (C_{t0} - C_0)}{NS_p t}$$

Here, C_0 is the original concentration of the dissolved oxygen in the solution without UV irradiation, C_{t0} and C_t are the oxygen concentrations found with only the H_2O_2 and the mixture, respectively, at time *t* under UV irradiation. *N* is the number of E-TiO_2 micromotors in the unit volume. S_p is the surface area of a micromotor.

2.6. Numerical simulations

The numerical simulation of the propagation and attenuation of light in the E-TiO_2 microparticles was performed *via* the full-wave optics and transient diffusion modules of the commercial COMSOL Multiphysics package. The wavelength of the plane light source in this simulation is 365 nm. The diameter and refractive index of the E-TiO_2 microspheres are 1 μm

and 2.7−0.15i and the perfected layers were set up to simulate an isolated sphere. Three different power inputs of 50, 500, and 590 mW were respectively studied here.

Nonelectrolyte (O_2 molecules) diffusiophoresis induced concentration gradients, fluid speed, and pressure distribution were simulated using the diffusions and creeping flow modules of the commercial COMSOL Multiphysics package. The simulation was built up by placing an E-TiO_2 micromotor on a glass substrate (100 μm in width), which was immersed in the bottom of a 0.01 mm^2 square space which is filled with water. By quantitative measurement of dissolved oxygen due to the photocatalytic decomposition of H_2O_2, the flux of oxygen molecules (J_{O_2}) are 0.71 $\times 10^{-4}$ and 9.5$\times 10^{-4}$ mol/(m^2s) (Fig. S1) at I of 50 and 500 mW cm^{-2}, respectively. And the J_{O_2} at the I of 590 mW cm^{-2} was then calculated to be 14.5$\times 10^{-4}$ mol/(m^2s) according to the result in Fig. S1. From the analysis of the TEM figure, the motor model is approximately set to be that a solid sphere (diameter: 500 nm) attached to a 50 nm spherical shell. The surface mobility over the particle surface (b_p) is deduced to be 1×10^{-10} m^5 mol^{-1} s^{-1}, and the b_w is set to be 0.5b_p [50]. The diffusion coefficient of O_2 molecules in water is 1.97$\times 10^{-9}$ m^2 s^{-1} [14]. The reactions inside of the particles are not considered because it is not easy for the produced O_2 molecules to diffuse out of them and the induced surface osmosis can be neglected. The governing equations of the numerical simulations are given in Supplementary Information.

3. Results and discussion

To demonstrate the design strategy of the E-TiO_2 micromotors with multimodal motion behaviors, the eccentric core-in-hollow shell TiO_2 microspheres, which have a unique isotropic outer surface but inherent inner mass asymmetry, were fabricated at first by a simple solvothermal method followed by calcination (see details in the Experimental section) [48]. The

formation of the eccentric core-in-hollow shell structure is attributed to the typical Ostwald ripening process, in which the growth of the outer hollow shell is at the expense of the dissolution of the inner core, thereby generating an interior hollow space between the shell and the core [48]. Fig. 1A-C shows the structure of the obtained eccentric core-in-hollow shell TiO_2 microspheres. The SEM and TEM images (Fig. 1A and B) confirm that the particles are in spherical structures with an average diameter of 1 μm and with rough surfaces. In addition, they are anisotropic with a spherical inner core attached to one side of the hollow shell, with an average shell thickness of 50 nm. The XRD pattern (Fig. 1C) shows that the particles consist of a single component of anatase TiO_2. TiO_2 is one of the most common photocatalysts with high stability and excellent photocatalytic activity. Upon UV illumination, TiO_2 micromotors catalyze the decomposition of H_2O_2 (fuel) as follows: [51]

$$TiO_2 + hv \rightarrow h^+ + e^- \quad (1)$$

$$H_2O_2 + 2h^+ \rightarrow O_2 + 2H^+ \quad (2)$$

$$H_2O_2 + 2e^- + 2H^+ \rightarrow 2H_2O \quad (3)$$

The molecular product (O_2) then induces non-electrolyte diffusiophoresis as the dominant propulsion mechanism.

We first describe the multiple motion behavior of E-TiO_2 micromotors, from negative phototaxis to random propulsion, upon sidewise UV light irradiation. The specific experimental setup is demonstrated in Fig. S2. In a typical experiment, the E-TiO_2 micromotors are dispersed in the aqueous medium (5.0 wt.% H_2O_2), and they only exhibit Brownian motion with UV light off (Fig. 1D(i) and Video S1). To obtain a quantitative insight into the behaviors of micromotors, the trajectories are color-coded to record their time progression in 5 s intervals while tracking. Turning on the UV light from the side and adjusting the light intensity (I) to 50 mW cm^{-2}, the E-TiO_2 micromotors showed negative phototaxis (Fig. 1D(ii) and Video S1) that can be observed

from the color positions of the starting and ending points. At I of 150 mW cm^{-2}, the micromotor trajectories start to become more random in nature, as shown in Fig. 1D(iii). As I is increased, the motion of the E-TiO_2 micromotors becomes more diffusive with less directionality (Fig. 1D(iv)). Not only the motion behavior, but also the speed of E-TiO_2 micromotors can be precisely controlled by regulating I. Fig. 1E shows that the average speed of the microparticles gradually increases from 2.2 to 7.2 μm s^{-1} as I increases from 0 to 500 mW cm^{-2}.

The schematic diagram of an E-TiO_2 micromotor in the aforementioned experimental system is shown in Fig. 2A. Like other colloids whose densities are larger than water, the fabricated motors tend to reside near the substrate surface because of gravity sedimentation. Here, the particle gravity is considered to be completely compensated by thermal motion and the average particle height from the substrate is determined according to $h = K_BT/mg$, where mg represents the particle buoyant gravity [52]. The angle between the particle symmetry axis and the normal vector perpendicular to the substrate is defined as the orientation angle (θ) of the E-TiO_2 micromotor (Fig. 2A). Due to the asymmetric mass distribution, the E-TiO_2 micromotor would experience an intrinsic torque (T_0) once the motor axis deviated from the surface normal of the substrate (or $\theta \neq 0$). The maximum magnitude of T_0 was calculated to be 0.7×10^{-21} N·m at a θ of 90° according to the model given in Fig. 2A. This value is comparable to Brownian random torque (T_B, 10^{-21} N·m) estimated from the maximum magnitude of Brownian force ($F_B = k_BT/2r$) times r [53]. This suggests that Brownian random rotation of the motor in water is largely constrained by its asymmetric mass distribution and it prefers to have an orientation with the inner core downward (-90° < θ < 90°).

The time-averaged energy density of UV light with different I in an E-TiO_2 micromotor with a typical orientation (θ = 45°) was simulated using the COMSOL software [54]. At low I,

only a few photons can pass through the shell and reach the core (left panel of Fig. 2B), and a small number of photogenerated holes and electrons were generated in the core. Further, most of them would be consumed rapidly at the inner core surface by H_2O_2 (5 wt.%) inside the E-TiO_2 micromotor. As a result, few holes and electrons generated in the core can diffuse to the outer surface of the E-TiO_2 micromotor, and the photocatalytic reaction occurs predominantly on the illuminated outer surface. Under this condition, the produced O_2 molecules would mainly accumulate at the illuminated side of the E-TiO_2 micromotor (Fig. S3A), and the resulting O_2 gradient across the motor would induce a surface phoretic slip to drive it with the shadowed side forward near the substrate (Fig. 2Ca). The driving force generated by the phoretic flow can be decomposed into a horizontal driving force F_x (1.3×10^{-14} N) to propel the motor moving along the substrate and a vertical downward force F_y (5.9×10^{-15} N) which pushes the motor close to the substrate. The average height h of the motor to the substrate can be estimated to be about 145 nm according to $h = K_BT/(mg + F_y)$ [52].

In contrast, at a high I, enough photons can penetrate the shell (right panel of Fig. 2B), and the generated electrons and holes in the core can migrate to the nearby outer surface (the diffusion length of photogenerated charges can reach tens of micrometers and participate in the photocatalytic reactions there [55]. Thus, the inherent mass asymmetry now influences the motion behavior of the E-TiO_2 micromotor. To verify this, the phoretic flow field (u) around an E-TiO_2 micromotor with a θ of 45° at the high I of 500 mW cm^{-2} was simulated (Fig. 2Cb). Due to the strong F_y (4.5×10^{-14} N) originating from the high O_2 flux, the motor sinks to a position with an h of 75 nm (Fig. 2Cb) to the substrate, and thus the produced O_2 becomes highly concentrated in the confined space between the motor and the substrate on the core side (i.e., the shadowed side). The high concentration of O_2 will then induce a lateral phoretic flow toward the

confined space along the substrate on the core side, resulting in a high local pressure (p, color background in Fig. 2Cd) there. Consequently, different from the negative phototaxis in the $+x$ direction at low I (e.g. 50 mW cm^{-2}, Fig. 2Ca), the motor with the same orientation ($\theta = 45°$) can now move in the opposite direction ($-x$ direction, Fig. 2Cb) near the substrate under the F_x of -5.5 × 10^{-14} N (Fig. 2D). This reversal in motion direction (or the direction of F_x) highlights the contribution of the mass asymmetry to the propulsion and the orientation-dependent directionality of E-TiO_2 micromotors at high I. As a result, similar to the traditional asymmetric Janus-structured micro/nanomotors [56-58], the E-TiO_2 motors perform a random motion because of their constantly varying orientation (θ) due to Brownian rotations. It is worth noting that the horizontal driving force F_x at low I mainly resulted from the phoretic force *via* the slip velocity on the motor (Fig. 2Cc), while that at high I comes from the fluid pressure predominantly induced by the accumulated product, O_2 (Fig. 2Cd).

To summarize the behavior of the E-TiO_2 motors with varying I, under a sidewise UV irradiation with low I, the micromotors can be treated as isotropic spheres and they undergo directional negative phototaxis due to the persistent chemiosmotic slip toward the illuminated side of the motor regardless of their orientation (Fig. 2E) [14]. In contrast, the E-TiO_2 micromotors tend to move randomly at a high I (Fig. 2F) because of the contribution of the core to the propulsion and the orientation-dependent motion directionality.

When the H_2O_2 fuel concentration (C_f) changes, the E-TiO_2 micromotors irradiated vertically from the bottom of the substrate can switch their motion behavior between negative photogravitaxis and random propulsion, as illustrated in Fig. 3. In detail, at a low C_f (0.01 wt.% H_2O_2) and an I of 590 mW cm^{-2}, the microparticles gradually move out of focus as they move upwards against gravity (0 - 50 s in Fig. 3C and Video S2). The trajectories of two E-TiO_2

micromotors are shown in Fig. 3D, indicating the negative photogravitactic migration in the $+z$ direction (ca. 0.12 μm s^{-1}) and with random movement in the 2D horizontal plane. In contrast, these micromotors only exhibited continuous, wall-bound stochastic motion in the 2D plane when C_f was increased from 0.01 to 5 wt.%, either illuminated vertically from the bottom (Fig. 3B and 3E) or the above of the substrate (Fig. S4). The experiments with vertical upward light illumination were also conducted at a low C_f (0.01 wt.%) and lower values of I (80 and 350 mW cm^{-2}). Only a few micromotors moved up at I = 80 mW cm^{-2} while many more moved up at I = 350 mW cm^{-2}. As expected, the speed of E-TiO_2 micromotors at a high C_f can be controlled by varying I, as demonstrated in Fig. 3F, where the speed increased from 6.5 to 9.5 μm s^{-1} when I was enhanced from 350 to 590 mW cm^{-2}.

To understand the switchable motion behavior of E-TiO_2 micromotors upon vertical UV illumination from the bottom, we focus on the orientation angle θ in the absence and presence of UV light. Fig. 4A and 4B show the time-lapse microscopic images through a 100× objective at a rate of 18 frames per second, describing the in-plane orientation of the motors (taken from Video S4). The dark and light colors correspond to the core and hollow shell, respectively. In the absence of light, irrespective of C_f, the E-TiO_2 micromotor undergoes continuous Brownian rotations but has favorable orientations with the core downward (upper panels in Fig. 4A and 4B). When the vertical UV illumination was turned on, at a low C_f (0.01 wt.% H_2O_2), the similar constantly varying but preferred core-downward orientation ($-90^o < \theta < 90^o$) of the E-TiO_2 micromotor was observed, and it gradually moved vertically upwards away from light (lower panel in Fig. 4A, Fig. S5 and Video S4) [50]. In contrast, the E-TiO_2 micromotors always move near the substrate with a stable core-sideward orientation ($\theta \approx 90°$) when C_f was increased to 5 wt.% (Fig. 4B and Video S4).

Modeling helped to understand the above behavior. Upon vertical UV light irradiation from the bottom, due to the relative higher photocatalytic activity of the core side, the motor tends to rotate its core side away from the substrate when the motor axis deviated from the surface normal of the substrate ($\theta \neq 0^o$), as evidenced by the simulated flow field (u) (Fig. 4C) and the correspondingly generated phoretic torque (T) (Fig. 4D) around an E-TiO_2 micromotor. Nevertheless, the magnitude of T acting on the motor (blue curve in Fig. 4D) is too low to overcome its intrinsic torque (black curve in Fig. 4D) at low C_f (0.01 wt.%) even at a θ of 15°, and thus it always moves vertically upwards away from light (negative photogravitaxis). In stark contrast, the magnitude of T of the motor reaches a maximum value as high as 9.45×10^{-20} N·m when θ = -30° (or θ = 30°) at the high C_f (5 wt.%) (red curve in Fig. 4D). Even though gradually weakening as the θ deviates from -30° (or θ = 30°), the phoretic torque T (0.4×10^{-21} N·m) on the motor is still comparable to T_0 (0.7×10^{-21} N·m) even at the θ of 90° (or -90°). Hence, the E-TiO_2 micromotors prefer to move with a core-sideward orientation ($\theta \approx$ -90° or 90°) near the substrate at the high C_f (5 wt.%). In addition, the hydrodynamic interactions between the active motor and the substrate may also facilitate its 2D motion near the substrates [50,59-62]. The multimodal motion behavior of the E-TiO_2 micromotors at different C_f are summarized in Fig. 4E and 4F. Under vertically upward UV illumination, the motors tend to perform negative photogravitaxis due to their core-downward orientation under the dominant intrinsic torque at the low C_f (Fig. 4E), while they prefer to move randomly in the 2D plane (near the substrate) in a core-sideward orientation ($\theta \approx$ -90° or 90°) because of their apparent reorientation under the overwhelming phoretic torque at the high C_f (Fig. 4F).

4. Conclusion

We have shown photochemically-powered micromotors with the motion behavior actively adjusted to environmental cues. Based on the inherent mass asymmetry, single-component eccentric core-in-hollow shell TiO_2 (E-TiO_2) micromotors in hydrogen peroxide (H_2O_2) solution under UV irradiation can display negative phototaxis, negative photogravitaxis, and random diffusive propulsion, depending on the UV light intensity (I) and the H_2O_2 concentration (C_f). When illuminated from one side with a low I, the E-TiO_2 micromotors act as isotropic microspheres and undergo negative phototaxis. Once I is increased, the photocatalysis by the eccentric core of the micromotors becomes remarkable, resulting in random Brownian superdiffusion. In another example, when the UV light is applied vertically from the bottom, either negative photogravitaxis or Brownian superdiffusion can be observed depending on whether the C_f is low or high. The experimental observations were supported by numerical simulations. This ability to control the motile behavior "on the fly" by two different inputs overcomes an important barrier to the design of micro/nanomotors that can serve multiple functions, such as search and delivery. The directional taxis of the motors would allow them to quickly move to a target area; subsequently switching the motion to superdiffusion will then enable the motors to efficiently deliver cargoes over the entire area.

Figures

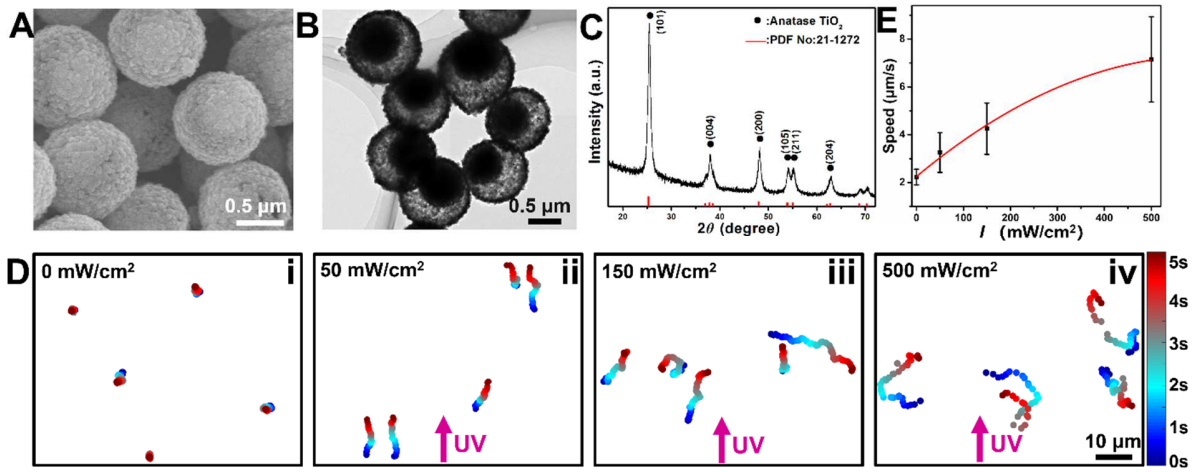

Fig. 1. The characterization and motion analysis of E-TiO_2 micromotors when UV light is irradiated from one side. (A-C) Scanning electron microscopy (SEM) image (A), Transmission electron microscopy (TEM) image (B), and X-ray diffraction (XRD) pattern (C) of the typical E-TiO_2 microspheres, respectively. (D) The motion trajectories of E-TiO_2 micromotors over 5 s in the aqueous medium with 5.0 wt.% H_2O_2 under different strengths of UV irradiation, obtained from Video S1. The coded different color records the time progression. (E) Average speed of the E-TiO_2 micromotors at different *I*, which was determined by tracking 15 microparticles. The concentration of H_2O_2 in the medium is 5.0 wt.%.

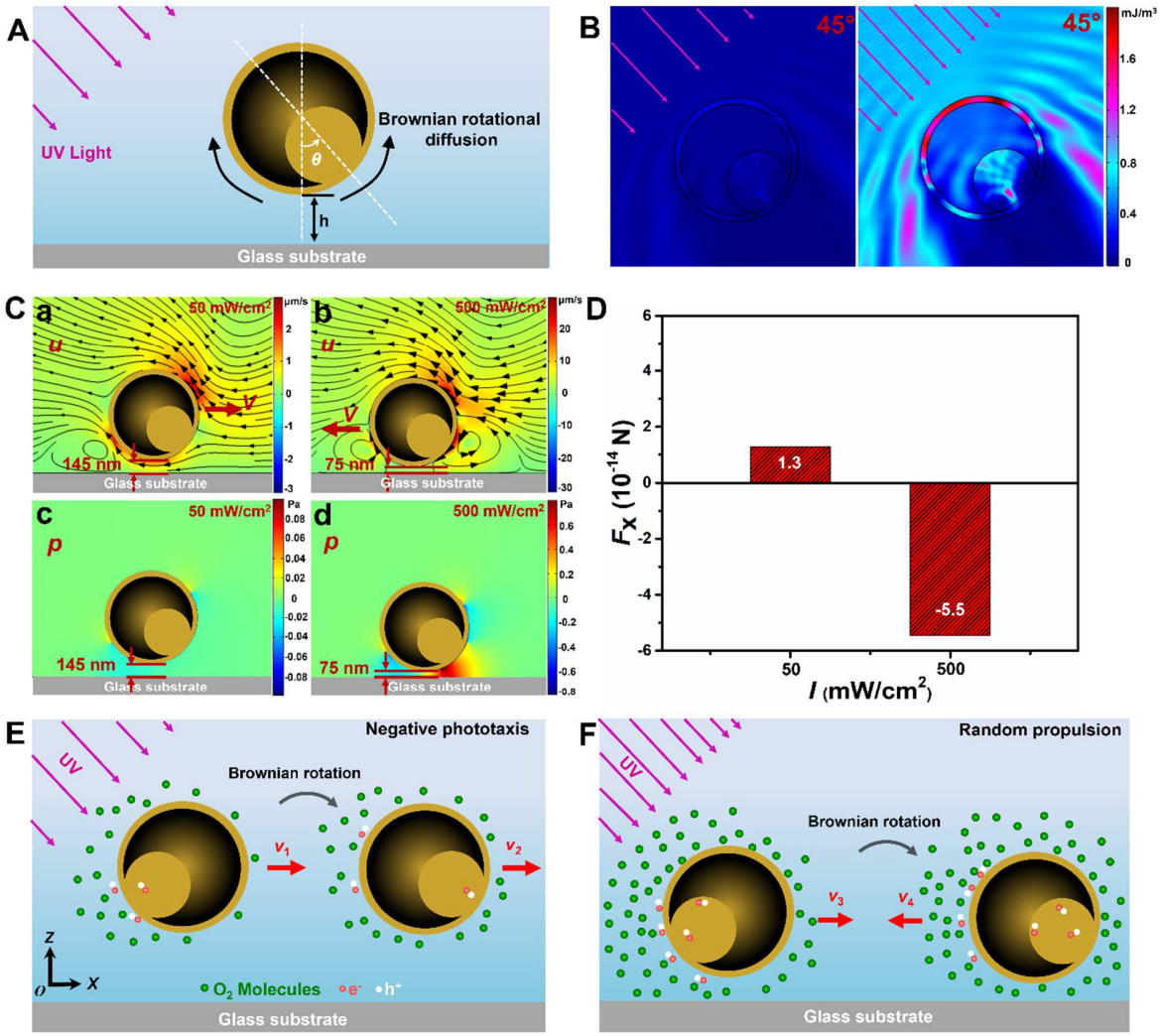

Fig. 2. The numerical simulations, calculation, and schematic diagrams toward the motion mechanism of the E-TiO_2 micromotors under sidewise UV irradiation at different *I*. (A) Schematic illustration of the Brownian rotational diffusion and suspension height (*h*) of an E-TiO_2 micromotor in the aqueous medium with 5.0 wt.% H_2O_2 under UV irradiation. The parameter θ describes the polar angle between the particle symmetry axis and the normal vector perpendicular to the substrate. (B) Simulated results of the time-averaged energy density of UV light in the E-TiO_2 micromotors ($\theta = 45°$) with different *I*. The power inputs were set as 50 (left panel), and 500 mW (right panel), respectively. The wavelength and incident angle of UV light are 365 nm and 45°. (C) The simulated velocity in the *x* direction and the streamlines (black

curves) of the hydrodynamic flow (a, b), and the pressure (P) on the particle surfaces (c, d) induced by the ∇C along the surface of the particles and the interactions between particles and substrate with different I, (a, c) 50 mW cm^{-2} and (b, d) 500 mW cm^{-2}. The red arrows in a and b indicate the instantaneous motion directions of the respective motors. (D) The calculated horizontal driving force (F_x) acting on the motors under UV irradiation at different I of 50 and 500 mW cm^{-2}. (E) The negative phototaxis mechanism of E-TiO_2 micromotors at a low I (under 50 mW cm^{-2}). (F) The random propulsion mechanism of E-TiO_2 micromotors at a high I (over 150 mW cm^{-2}). Red arrows represent the motion directions of the micromotors at different states. The yellow body in the diagram indicates the E-TiO_2 micromotor while the black represents the hollow part. All diagrams are demonstrated from the X-Z plane (perpendicular to the substrate, as depicted in E). Purple arrows indicate the incident direction of the UV light.

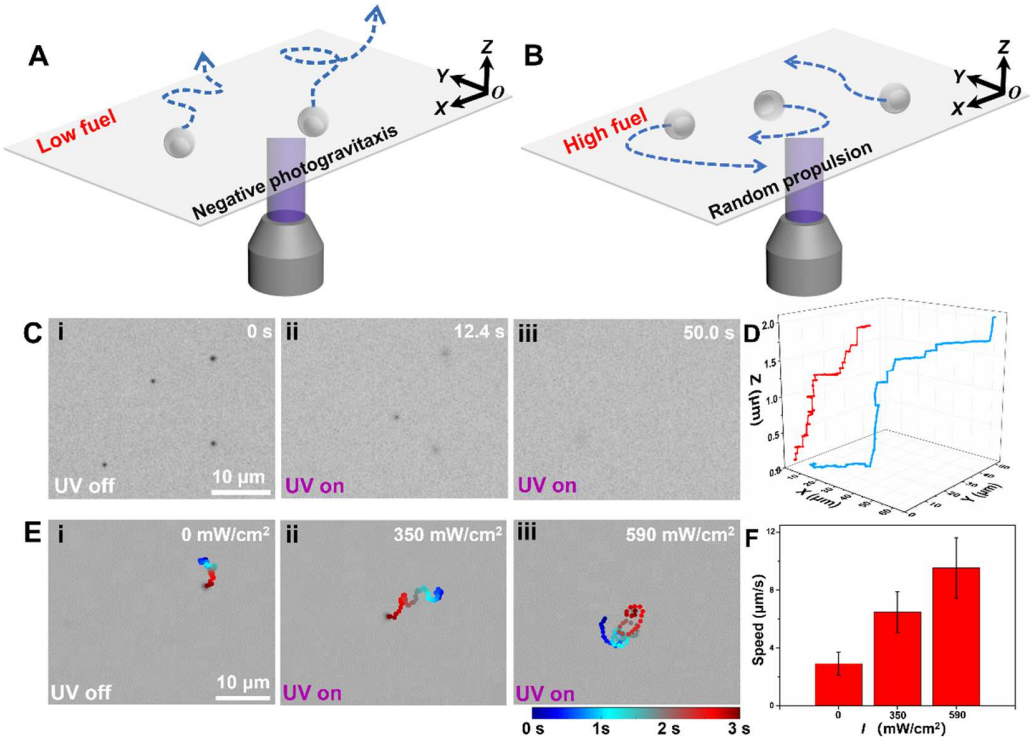

Fig. 3. Negative photogravitaxis and random propulsion of E-TiO_2 micromotors. (A, B) The schematic diagram depicting the motion behavior variation of E-TiO_2 micromotors with *I* when UV light is applied vertically from the bottom. (C) (i-iii) Time-lapse snapshots of the motions of the E-TiO_2 micromotors with 0.01 wt.% H_2O_2 at $I = 590$ mW cm^{-2}; images are taken from Video S2. (D) The motion trajectories of 2 micromotors in three-dimension (3D) space in 15.5 s. The ranges of *X* axis and *Y* axis correspond to the length and width of i-iii (C). (E) Motion trajectories of an E-TiO_2 micromotor over 3 s within 5.0 wt.% H_2O_2 at different *I*; images are taken from Video S3. The coded color records the time progression. (F) Average speed of the E-TiO_2 micromotors at different *I* with 5.0 wt.% H_2O_2 as fuel, which was calculated by tracking 15 microparticles.

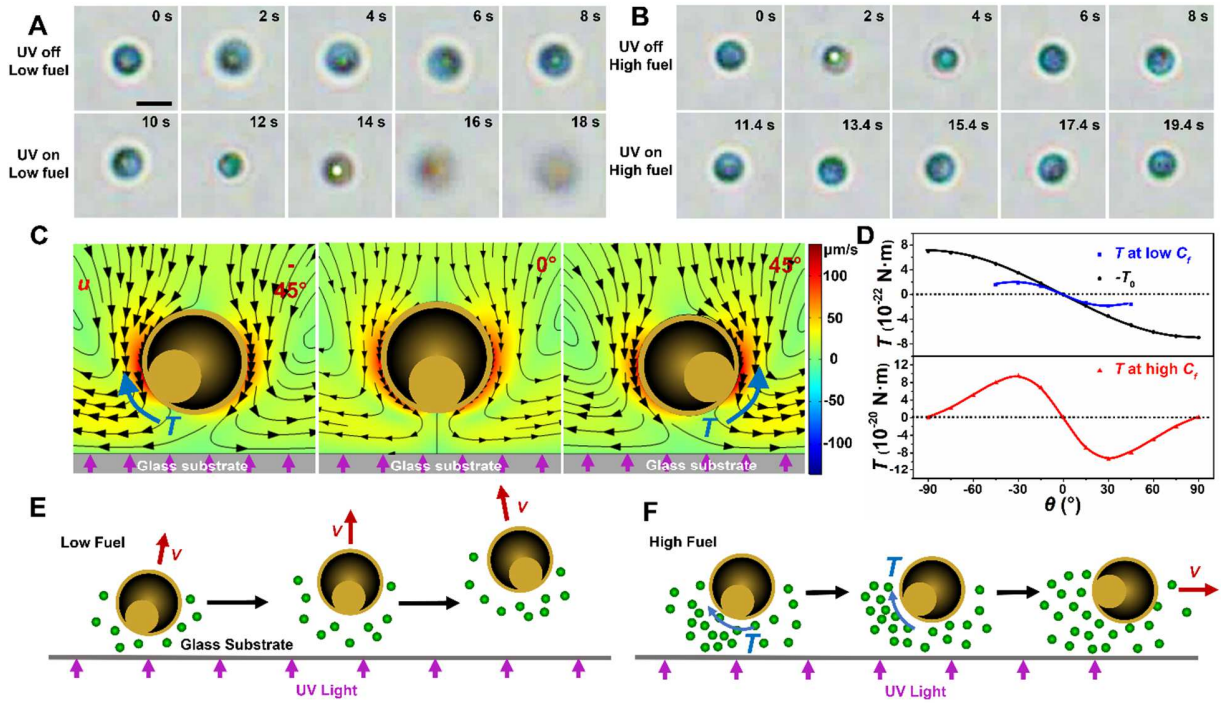

Fig. 4. Brownian rotational change, underlying mechanism analysis of an E-TiO_2 micromotor under vertical UV illumination with different I and C_f. (A, B) Images taken from an optical microscopy video (Video S4) depict the states (θ) of E-TiO_2 micromotors at low C_f (A, 0.01 wt.% H_2O_2) and high C_f (B, 5 wt.% H_2O_2), respectively; the shells and cores of the colloidal particles appear bright and dark, respectively. I: 590 mW cm^{-2}, scale bar: 1 μm. (C) The simulated velocity along the x direction and the streamlines (black curves) of the hydrodynamic flow (u) induced by the ∇C along the surface of the particles at different θ (-45°, 0°, 45°) at high C_f (5 wt.% H_2O_2). (D) The calculated vertical torque (T) of the E-TiO_2 micromotor at different θ ($90° \leq \theta \leq 90°$) under UV irradiation at high C_f (5 wt.% H_2O_2, red curve) and low C_f (0.01 wt.% H_2O_2, blue curve). I: 590 mW cm^{-2}. The black curve indicates the intrinsic torque ($-T_0$) of the E-TiO_2 micromotor at different θ ($90° \leq \theta \leq 90°$). (E, F) The motility mechanism of E-TiO_2 micromotors at low C_f (E) and high C_f (F). The black and blue arrows represent the switch

between different states and the rotation trends of the motors, respectively. And the red and purple arrows indicate the respective motion direction of the motor and the incident direction of the UV light.

Author Contributions

F.M., J.G., and A.S. conceived and designed this work. J.Z., F.M., S.T. and J.K. performed the experiments. F.M. and J.Z. carried out the modelling. All the authors contributed to the discussion of results and the writing of the manuscript. All authors have given approval to the final version of the manuscript.

Declaration of Competing Interest

The authors declare no competing financial interest.

Acknowledgment

Fangzhi Mou and Jianguo Guan are grateful for the financial support from the National Natural Science Foundation of China (21875175, 52073222 and 51521001) and the Natural Science Foundation of Hubei Province (2019CFA048). Jiaqi Song, Joshua E. Kauffman and Ayusman Sen acknowledge financial support by the Department of Energy, Office of Basic Energy Sciences (DOE-DE-SC0020964). Jianhua Zhang acknowledges the Scholarship Fund from China Scholarship Council (CSC).

References

[1] J. Wang, W. Gao, Nano/microscale motors: biomedical opportunities and challenges, ACS Nano 6 (2012) 5745-5751.

[2] M. Safdar, S. U. Khan, J. Janis, Progress toward catalytic micro- and nanomotors for biomedical and environmental applications, Adv. Mater. 30 (2018) 1703660.

[3] M. Luo, Y. Feng, T. Wang, J. Guan, Micro-/nanorobots at work in active drug delivery, Adv. Funct. Mater. 28 (2018) 1706100.

[4] M. Zarei, M. Zarei, Self-propelled micro/nanomotors for sensing and environmental remediation, Small 14 (2018) 1800912.

[5] J. Li, B. Esteban-Fernández de Ávila, W. Gao, L. Zhang, J. Wang, Micro/nanorobots for biomedicine: delivery, surgery, sensing, and detoxification, Sci. Robot. 2 (2017) eaam6431.

[6] K. Gentile, A. Somasundar, A. Bhide, A. Sen, Chemically powered synthetic “living” systems, Chem 6 (2020) 2174-2185.

[7] H. Ye, Y. Wang, D. Xu, X. Liu, S. Liu, X. Ma, Design and fabrication of micro/nano-motors for environmental and sensing applications, Appl. Mater. Today 23 (2021) 101007.

[8] X. Fan, Q. Hao, M. Li, X. Zhang, X. Yang, Y. Mei, T. Qiu, Hotspots on the move: active molecular enrichment by hierarchically structured micromotors for ultrasensitive SERS sensing, ACS Appl. Mater. Interfaces 12 (2020) 28783–28791.

[9] J. Li, V. V. Singh, S. Sattayasamitsathit, J. Orozco, K. Kaufmann, R. Dong, W. Gao, B. Jurado-Sanchez, Y. Fedorak, J. Wang, Water-driven micromotors for rapid photocatalytic degradation of biological and chemical warfare agents, ACS Nano 8 (2014) 11118-11125.

[10] B. Jurado-Sánchez, S. Sattayasamitsathit, W. Gao, L. Santos, Y. Fedorak, V. V. Singh, J. Orozco, M. Galarnyk, J. Wang, Self-propelled activated carbon Janus micromotors for efficient water purification, Small 11 (2015) 499-506.

[11] F. Mou, L. Kong, C. Chen, Z. Chen, L. Xu, J. Guan, Light-controlled propulsion, aggregation and separation of water-fuelled TiO_2/Pt Janus submicromotors and their "on-the-fly" photocatalytic activities, Nanoscale 8 (2016) 4976-4983.

[12] L. s. Soler, V. Magdanz, V. M. Fomin, S. Sanchez, O. G. Schmidt, Self-propelled micromotors for cleaning polluted water, ACS Nano 7 (2013) 9611-9620.

[13] B. Dai, J. Wang, Z. Xiong, X. Zhan, W. Dai, C. C. Li, S. P. Feng, J. Tang, Programmable artificial phototactic microswimmer, Nat. Nanotechnol. 11 (2016) 1087-1092.

[14] C. R. Chen, F. Mou, L. Xu, S. Wang, J. Guan, Z. Feng, Q. Wang, L. Kong, W. Li, J. Wang, Q. Zhang, Light-steered isotropic semiconductor micromotors, Adv. Mater. 29 (2017) 1603374.

[15] H. Xu, M. Medina-Sanchez, V. Magdanz, L. Schwarz, F. Hebenstreit, O. G. Schmidt, Sperm-hybrid micromotor for targeted drug delivery, ACS Nano 12 (2018) 327-337.

[16] H. Xu, M. Medina-Sanchez, O. G. Schmidt, Magnetic micromotors for multiple motile sperm cells capture, transport, and enzymatic release, Angew. Chem. Int. Ed. 59 (2020) 15029-15037.

[17] Y. Feng, Y. Yuan, J. Wan, C. Yang, X. Hao, Z. Gao, M. Luo, J. Guan, Self-adaptive enzyme-powered micromotors with switchable propulsion mechanism and motion directionality, Appl. Phys. Rev. 8 (2021) 011406.

[18] A. Somasundar, S. Ghosh, F. Mohajerani, L. N. Massenburg, T. Yang, P. S. Cremer, D. Velegol, A. Sen, Positive and negative chemotaxis of enzyme-coated liposome motors, Nat. Nanotechnol. 14 (2019) 1129–1134.

[19] H. Zhou, C. C. Mayorga-Martinez, S. Pane, L. Zhang, M. Pumera, Magnetically driven micro and nanorobots, Chem. Rev. 121 (2021) 4999-5041.

[20] S. Du, H. Wang, C. Zhou, W. Wang, Z. Zhang, Motor and rotor in one: light-active ZnO/Au twinned rods of tunable motion modes, J. Am. Chem. Soc. 142 (2020) 2213-2217.

[21] J. Zhang, X. Zheng, H. Cui, Z. Silber-Li, The self-propulsion of the spherical Pt–SiO_2 Janus micro-motor, Micromachines 8 (2017) 123.

[22] G. M. Viswanathan, Fish in lévy-flight foraging, Nature 465 (2010) 1018–1019.

[23] F. Bartumeus, M. G. E. d. Luz, G. M. Viswanathan, J. Catalan, Animal search strategies: a quantitative random-walk analysis, Ecology 86 (2005) 3078-3087.

[24] F. Novotný, H. Wang, M. Pumera, Nanorobots: machines squeezed between molecular motors and micromotors, Chem 6 (2020) 867-884.

[25] B. Wang, K. Kostarelos, B. J. Nelson, L. Zhang, Trends in micro‐/nanorobotics: materials development, actuation, localization, and system integration for biomedical applications, Adv. Mater. 33 (2020) 2002047.

[26] L. Xu, F. Mou, H. Gong, M. Luo, J. Guan, Light-driven micro/nanomotors: from fundamentals to applications, Chem. Soc. Rev. 46 (2017) 6905-6926.

[27] F. Mou, J. Zhang, Z. Wu, S. Du, Z. Zhang, L. Xu, J. Guan, Phototactic flocking of photochemical micromotors, iScience 19 (2019) 415-424.

[28] T. Patino, N. Feiner-Gracia, X. Arque, A. Miguel-Lopez, A. Jannasch, T. Stumpp, E. Schaffer, L. Albertazzi, S. Sanchez, Influence of enzyme quantity and distribution on the self-propulsion of non-Janus urease-powered micromotors, J. Am. Chem. Soc. 140 (2018) 7896-7903.

[29] M. Xuan, R. Mestre, C. Gao, C. Zhou, Q. He, S. Sanchez, Noncontinuous super-diffusive dynamics of a light-activated nanobottle motor, Angew. Chem. Int. Ed. 57 (2018) 6838-6842.

[30] B. Xu, B. Zhang, L. Wang, G. Huang, Y. Mei, Tubular micro/nanomachines: from the basics to recent advances, Adv. Funct. Mater. 28 (2018) 1705872.

[31] J. Zheng, B. Dai, J. Wang, Z. Xiong, Y. Yang, J. Liu, X. Zhan, Z. Wan, J. Tang, Orthogonal navigation of multiple visible-light-driven artificial microswimmers, Nat. Commun. 8 (2017) 1438.

[32] J. Zhang, F. Mou, Z. Wu, S. Tang, H. Xie, M. You, X. Liang, L. Xu, J. Guan, Simple-structured micromotors based on inherent asymmetry in crystalline phases: design, large-scale preparation, and environmental application, ACS Appl. Mater. Interfaces 11 (2019) 16639-16646.

[33] C. Zhou, X. Chen, Z. Han, W. Wang, Photochemically excited, pulsating Janus colloidal motors of tunable dynamics, ACS Nano 13 (2019) 4064–4072.

[34] Z. Xiao, J. Chen, S. Duan, X. Lv, J. Wang, X. Ma, J. Tang, W. Wang, Bimetallic coatings synergistically enhance the speeds of photocatalytic TiO_2 micromotors, Chem. Commun. 56 (2020) 4728-4731.

[35] S. Tang, F. Zhang, J. Zhao, W. Talaat, F. Soto, E. Karshalev, C. Chen, Z. Hu, X. Lu, J. Li, Z. Lin, H. Dong, X. Zhang, A. Nourhani, J. Wang, Structure‐dependent optical modulation of propulsion and collective behavior of acoustic/light‐driven hybrid microbowls, Adv. Funct. Mater. 29 (2019) 1809003.

[36] K. Xiong, L. Xu, J. Lin, F. Mou, J. Guan, Mg-based micromotors with motion responsive to dual stimuli, Research 2020 (2020) 6213981.

[37] W. Wang, Z. Wu, X. Lin, T. Si, Q. He, Gold-nanoshell-functionalized polymer nanoswimmer for photomechanical poration of single-cell membrane, J. Am. Chem. Soc. 141 (2019) 6601-6608.

[38] R. Dong, Q. Zhang, W. Gao, A. Pei, B. Ren, Highly efficient light-driven TiO_2-Au Janus micromotors, ACS Nano 10 (2016) 839-844.

[39] D. P. Singh, U. Choudhury, P. Fischer, A. G. Mark, Non-equilibrium assembly of light-activated colloidal mixtures, Adv. Mater. 29 (2017) 1701328.

[40] W. F. Paxton, K. C. Kistler, C. C. Olmeda, A. Sen, S. K. S. Angelo, Y. Cao, T. E. Mallouk, P. E. Lammert, V. H. Crespi, Catalytic nanomotors: autonomous movement of striped nanorods, J. Am. Chem. Soc. 126 (2004) 13424-13431.

[41] A. A. Solovev, Y. Mei, E. Bermudez Urena, G. Huang, O. G. Schmidt, Catalytic microtubular jet engines self-propelled by accumulated gas bubbles, Small 5 (2009) 1688-1692.

[42] Y. Ji, X. Lin, H. Zhang, Y. Wu, J. Li, Q. He, Thermoresponsive polymer brush modulation on the direction of motion of phoretically driven Janus micromotors, Angew. Chem. Int. Ed. 58 (2019) 4184-4188.

[43] F. Mou, Y. Li, C. Chen, W. Li, Y. Yin, H. Ma, J. Guan, Single-component TiO_2 tubular microengines with motion controlled by light-induced bubbles, Small 11 (2015) 2564-2570.

[44] K. Villa, F. Novotny, J. Zelenka, M. P. Browne, T. Ruml, M. Pumera, Visible-light-driven single-component $BiVO_4$ micromotors with the autonomous ability for capturing microorganisms, ACS Nano 13 (2019) 8135-8145.

[45] K. Villa, C. L. Manzanares Palenzuela, Z. Sofer, S. Matejkova, M. Pumera, Metal-free visible-light photoactivated C_3N_4 bubble-propelled tubular micromotors with inherent fluorescence and on/off capabilities, ACS Nano 12 (2018) 12482–12491.

[46] F. Mushtaq, H. Torlakcik, M. Hoop, B. Jang, F. Carlson, T. Grunow, N. Läubli, A. Ferreira, X. Z. Chen, B. J. Nelson, S. Pané, Motile piezoelectric nanoeels for targeted drug delivery, Adv. Funct. Mater. 29 (2019) 1808135.

[47] J. Yu, D. Jin, K. F. Chan, Q. Wang, K. Yuan, L. Zhang, Active generation and magnetic actuation of microrobotic swarms in bio-fluids, Nat. Commun. 10 (2019) 5631.

[48] Z. Q. Li, W. C. Chen, F. L. Guo, L. E. Mo, L. H. Hu, S. Y. Dai, Mesoporous TiO_2 yolk-shell microspheres for dye-sensitized solar cells with a high efficiency exceeding 11%, Sci. Rep. 5 (2015) 14178.

[49] J. Guan, F. Mou, Z. Sun, W. Shi, Preparation of hollow spheres with controllable interior structures by heterogeneous contraction, Chem. Commun. 46 (2010) 6605-6607.

[50] D. P. Singh, W. E. Uspal, M. N. Popescu, L. G. Wilson, P. Fischer, Photogravitactic microswimmers, Adv. Funct. Mater. 28 (2018) 1706660.

[51] J. Zhang, J. Song, F. Mou, J. Guan, A. Sen, Titania-based micro/nanomotors: design principles, biomimetic collective behavior, and applications, Trends Chem. 3 (2021) 387-401.

[52] M. Driscoll, B. Delmotte, M. Youssef, S. Sacanna, A. Donev, P. Chaikin, Unstable fronts and motile structures formed by microrollers, Nat. Phys. 13 (2016) 375-379.

[53] A. Barik, X. Chen, S.-H. Oh, Ultralow-power electronic trapping of nanoparticles with sub-10 nm gold nanogap electrodes, Nano Lett. 16 (2016) 6317-6324.

[54] B. Jang, W. Wang, S. Wiget, A. J. Petruska, X. Chen, C. Hu, A. Hong, D. Folio, A. Ferreira, S. Pane, B. J. Nelson, Catalytic locomotion of core-shell nanowire motors, ACS Nano 10 (2016) 9983-9991.

[55] W. H. Leng, P. R. F. Barnes, M. Juozapavicius, B. C. O'Regan, J. R. Durrant, Electron diffusion length in mesoporous nanocrystalline TiO_2 photoelectrodes during water oxidation, J. Phys. Chem. Lett. 1 (2010) 967-972.

[56] C. Zhou, H. P. Zhang, J. Tang, W. Wang, Photochemically powered AgCl Janus micromotors as a model system to understand ionic self-diffusiophoresis, Langmuir 34 (2018) 3289-3295.

[57] B. Jang, A. Hong, H. E. Kang, C. Alcantara, S. Charreyron, F. Mushtaq, E. Pellicer, R. Buchel, J. Sort, S. S. Lee, B. J. Nelson, S. Pane, Multiwavelength light-responsive Au/B-TiO_2 Janus micromotors, ACS Nano 11 (2017) 6146-6154.

[58] W. Gao, X. Feng, A. Pei, Y. Gu, J. Li, J. Wang, Seawater-driven magnesium based Janus micromotors for environmental remediation, Nanoscale 5 (2013) 4696-4700.

[59] S. Das, A. Garg, A. I. Campbell, J. Howse, A. Sen, D. Velegol, R. Golestanian, S. J. Ebbens, Boundaries can steer active Janus spheres, Nat. Commun. 6 (2015) 8999.

[60] J. Simmchen, J. Katuri, W. E. Uspal, M. N. Popescu, M. Tasinkevych, S. Sanchez, Topographical pathways guide chemical microswimmers, Nat. Commun. 7 (2016) 10598.

[61] W. E. Uspal, M. N. Popescu, S. Dietrich, M. Tasinkevych, Self-propulsion of a catalytically active particle near a planar wall: from reflection to sliding and hovering, Soft Matter 11 (2015) 434-438.

[62] C. Liu, C. Zhou, W. Wang, H. P. Zhang, Bimetallic microswimmers speed up in confining channels, Phys. Rev. Lett. 117 (2016) 198001.

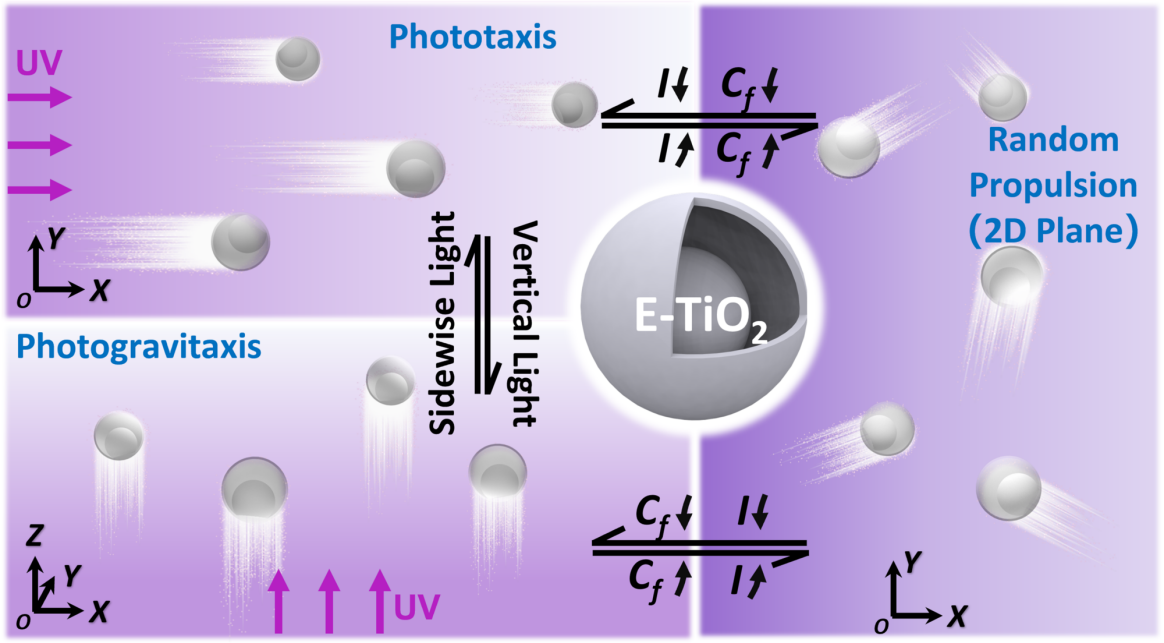
Phototaxis
UV
Y
X
o
I↓ C_f↓
I↑ C_f↑
Random
Propulsion
(2D Plane)
Sidewise Light
Vertical Light
E-TiO_2
Photogravitaxis
Z
Y
X
o
UV
C_f↓ I↓
C_f↑ I↑
Y
X
o